Research Article
Vol. 32, No. 9 / 22 Apr 2024 / Optics Express 15741
Optics EXPRESS

Performance of two semi-analytical algorithms in deriving water inherent optical properties in the Southern Ocean

YALONG ZHANG, XIAOLONG YU,* ZHONGPING LEE, SHAOLING SHANG, HANYANG QIAO, GONG LIN, AND WENDIAN LAI

State Key Laboratory of Marine Environmental Science, College of Ocean and Earth Sciences, Xiamen University, Xiamen 361101, China
*xlyu@xmu.edu.cn

Abstract: Remotely sensed inherent optical properties (IOPs) are key proxies for synoptic mapping of primary production and carbon export in the global ocean. However, the IOPs inversion algorithms are scarcely evaluated in the Southern Ocean (SO) because of limited field observations. In this study, the performance of two widely used semi-analytical algorithms (SAAs), *i.e.*, the quasi-analytical algorithm (QAA) and the generalized IOP model (GIOP), were evaluated using a compiled *in situ* bio-optical dataset in SO, as well as measurements from the Visible Infrared Imaging Radiometer Suite (VIIRS). Evaluations with *in situ* data show that QAA and GIOP have comparable performance in retrieving the total absorption coefficient ($a(\lambda)$), absorption coefficients of phytoplankton ($a_{\mathrm{ph}}(\lambda)$), and that of detritus and colored dissolved organic matter ($a_{\mathrm{dg}}(\lambda)$). Overall, it was found that remotely sensed $a(\lambda)$ and $a_{\mathrm{ph}}(\lambda)$ by both SAAs agreed well with field measurements, with the mean absolute percentage difference (MAPD) of derived $a(\lambda)$ and $a_{\mathrm{ph}}(\lambda)$ in the blue-green bands being ~20% and ~40%, respectively. However, derived $a_{\mathrm{dg}}(\lambda)$ by both SAAs were higher than the measured values at the lower end ($a_{\mathrm{dg}}(443) < \sim 0.01\ \mathrm{m}^{-1}$), but lower at the higher end ($a_{\mathrm{dg}}(443) > \sim 0.02\ \mathrm{m}^{-1}$), with MAPD of ~60%. Results of this effort suggest confident products of $a(\lambda)$ and $a_{\mathrm{ph}}(\lambda)$ from VIIRS in SO, but more dedicated efforts on the measurements and evaluation of $a_{\mathrm{dg}}(\lambda)$ in SO would be desired.

1. Introduction

The Southern Ocean (SO, south of 50°S), occupying ~10% of the world's ocean surface area, is a typical high-nutrient low-chlorophyll (HNLC) region [1], yet an important carbon sink, accounting for ~25% of the global ocean carbon dioxide uptake [2–4]. Currently, SO is undergoing unprecedented physical and chemical changes owing to global warming [5, 6]. Thus, there is a high demand for accurate assessments of primary production (PP) and carbon export in the region, as well as their long-term trends, so that a better understanding of the global carbon cycle and the response of SO to climate change can be possibly achieved. In this respect, satellite remote sensing is the only feasible means of evaluating PP and carbon export in the SO at large spatio-temporal scales.

Inherent optical properties (IOPs), including the spectral absorption and backscattering coefficients of different water components, determine light propagation within the water column and are closely related to the biogeochemical properties of the ocean. For instance, the absorption coefficient of phytoplankton ($a_{\mathrm{ph}}(\lambda)$, in m^{-1}) is particularly important for accurate estimation of PP [7–9], while the particulate backscattering coefficient ($b_{\mathrm{bp}}(\lambda)$, in m^{-1}) is a useful proxy for the concentration of particulate organic carbon (POC) in global oceans [10,11]. Colored dissolved organic matter (CDOM) contributes significantly to the dissolved organic carbon (DOC) pool, and absorption by CDOM ($a_{\mathrm{g}}(\lambda)$, in m^{-1}) is conventionally employed to remotely estimate

#515341
Journal © 2024
https://doi.org/10.1364/OE.515341
Received 7 Dec 2023; revised 22 Mar 2024; accepted 2 Apr 2024; published 15 Apr 2024

DOC concentration, especially in estuarine and coastal waters [12,13]. Previous studies have investigated the spatial-temporal variabilities of PP and POC using remotely sensed IOPs in the SO [9,10]; however, the robustness of satellite IOPs products has not been well investigated. There have been extensive efforts towards a better understanding of the remotely sensed chlorophyll-a concentration (Chla) in SO [14–17], while evaluations of the inversion algorithms for IOPs in SO have scarcely been reported.

Over the last several decades, several semi-analytical algorithms (SAAs) have been developed to derive IOPs from remote sensing reflectance ($R_{\mathrm{rs}}(\lambda)$, in sr^{-1}) measured *in situ* or by satellite [18–21]. These SAAs can be categorized into two types according to their bottom-up and top-down strategies [22]. Top-down algorithms, such as the widely-used quasi-analytical algorithm (QAA) [23], first estimate the total absorption coefficient $a(\lambda)$ and backscattering coefficient $b_{\mathrm{b}}(\lambda)$, and then partition $a(\lambda)$ and $b_{\mathrm{b}}(\lambda)$ into IOPs by different water components. Bottom-up algorithms, on the other hand, derive component IOPs simultaneously with assumed IOPs spectral shapes via spectral optimization [19,21,24,25], where the Generalized IOP model (GIOP) is mostly employed by the international community [19]. However, these SAAs were mainly developed based on measurements collected from mid-low-latitude oceans, and their applicability in polar oceans has not been systematically evaluated.

In this study, we compiled a relatively large bio-optical dataset for SO from both field campaigns and published data for the evaluations of SAAs in SO. The main objectives of this effort include (a) evaluating the performance of QAA and GIOP using both field- and satellite-measured R_{rs}, and (b) quantifying and discussing the uncertainties associated with the IOPs inversions in the SO, particularly for the inversion of absorption coefficients by different water constituents.

2. Data and methods

2.1. *in situ bio-optical dataset*

We compiled a dataset with a wide dynamic range of optical properties in SO from two sources. The first one includes field measurements in the coastal waters of the Antarctic continent obtained during the 38th Chinese National Antarctic Research Expedition aboard the R/V XUELONG icebreaker, which is hereafter termed SO-38. The sampling locations of SO-38 are illustrated in Fig. 1 with red circles. The second one was screened from version 3 of the global bio-optical dataset (GBD-v3) by Valente et al. [26] for measurements collected in the Southern Ocean (south of 60°S). For simplicity, the subset of GBD-v3 in the Southern Ocean is termed SO-GBD hereafter, while the rest measurements in GBD-v3 are termed GBD-Global. Note that the bio-optical measurements in SO-GBD were mainly collected from the nearby waters of the Antarctic Peninsula (see the blue squares in Fig. 1).

2.1.1. SO-GBD dataset

The GBD-v3 dataset can be accessed directly from https://doi.pangaea.de/10.1594/PANGAEA.941318, which is a compilation of several publicly available datasets, such as the Marine Optical Buoy (MOBY), SeaWiFS (Sea-Viewing Wide Field-of-View Sensor) Bio-optical Archive and Storage System (SeaBASS), and NASA bio-Optical Marine Algorithm Data set (NOMAD), for measurements from global oceans between 1997 and 2021 [26]. We first extracted matched R_{rs} and IOPs data from their respective spreadsheets aggregated within +/- 6 nm of the VIIRS bands. Measurements in the Southern Ocean (south of 60°S) were then screened. As our main focus is on the descriptions of the methods used to determine the bio-optical properties in SO-38, readers are referred to the corresponding references for the protocols and practices of the measurements of different bio-optical properties in SO-GBD [26]. In this effort, we further screened the R_{rs} measurements in SO-GBD using a quality assurance (QA) system [27]. Specifically, the QA system assigns a score between 0 and 1 to each R_{rs} spectrum, with 1 indicating perfect quality and

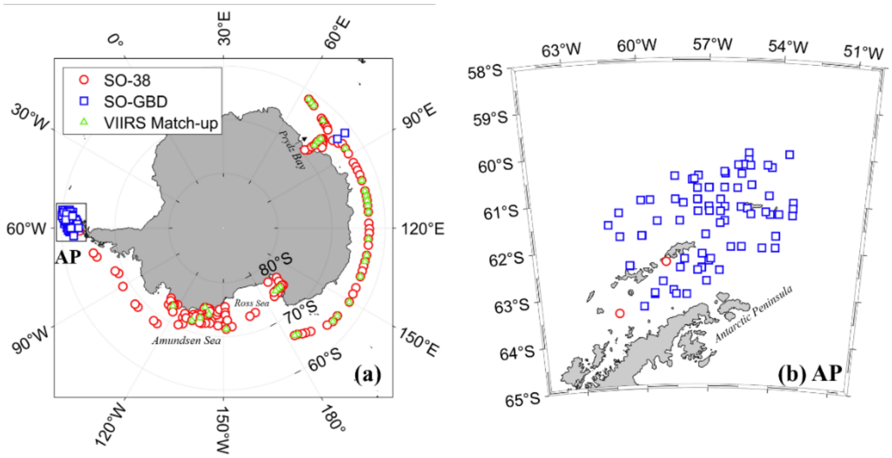

Fig. 1. Sampling locations of the compiled bio-optical dataset in the Southern Ocean with red circles and blue squares standing for measurements from the SO-38 and SO-GBD datasets, respectively. Panel (b) shows the sampling locations in the nearby waters of the Antarctic Peninsula (AP, the black box in panel (a)). The green triangles in panel (a) represent stations with matched measurements from both *in situ* and satellite.

0 for questionable spectrum. R_{rs} measurements with a QA score less than 0.5 were considered low quality and were removed from further analysis. As a result, the SO-GBD dataset consists of 88 valid measurements of $R_{rs}(\lambda)$ and $a_{ph}(\lambda)$ and 84 valid measurements of $a_{dg}(\lambda)$, with these measurements mainly collected between 2000 and 2007.

2.1.2. SO-38 dataset

The 38th Chinese National Antarctic Research Expedition was conducted between December 2021 and March 2022. During this expedition, radiometric measurements were carried out and water samples were collected at 142 stations, with their locations shown in Fig. 1(a). Note that at some of these stations, only water samples were collected, and radiometric measurements were absent due to rough sea conditions or bad weather.

a) Remote sensing reflectance

Spectral $R_{rs}(\lambda)$, defined as the ratio of water-leaving radiance ($L_w(\lambda)$, in $\mathrm{W \cdot m^{-2} \cdot nm^{-1} \cdot sr^{-1}}$) to the downwelling plane irradiance just above the sea surface ($E_d(\lambda, \mathrm{z}=0^+)$, in $\mathrm{W \cdot m^{-2} \cdot nm^{-1}}$), were measured using the above-water approach [28]. At each station, radiance measurements of the upwelling radiance above the surface ($L_u(\lambda)$), standard Spectralon plaque ($L_{plaque}(\lambda)$), and downwelling sky radiance ($L_{sky}(\lambda)$) were acquired sequentially using a GER1500 spectroradiometer (Spectra Vista Corporation, USA). Note that GER1500 covers a spectral range of 350–1050 nm with a spectral resolution of 3 nm. The viewing geometry of each radiance measurement conformed to NASA protocols [29]. The field-measured $R_{rs}(\lambda)$ were then calculated as

$$R_{rs}(\lambda) = \frac{\rho\left(L_u(\lambda) - r \times L_{sky}(\lambda)\right)}{\pi \times L_{plaque}(\lambda)} - \Delta, \tag{1}$$

where ρ is the reflectance of the spectralon plaque with a Lambertian surface (ρ ~0.5) and r is the air-water interface reflection coefficient, which was taken as 0.023 [30]. Δ ($\mathrm{sr^{-1}}$) accounts for the residual surface light (glint, etc.), and was corrected through an optimization scheme [31]. The corrected $R_{rs}(\lambda)$ were further screened for the QA score, and only high-quality R_{rs} spectra

(QA score ≥ 0.5) were retained (N = 78). Figure 2(a) shows the hyperspectral $R_{rs}(\lambda)$ spectra of SO-38, with the multispectral $R_{rs}(\lambda)$ measurements from SO-GBD provided for comparison.

b) Component absorption coefficients

The absorption coefficients of suspended particles ($a_p(\lambda)$), non-algae particles ($a_d(\lambda)$), and phytoplankton ($a_{ph}(\lambda)$) were determined using the filter-pad technique (QFT) [32]. Specifically, surface water samples were collected and immediately filtered through a 25 mm diameter Whatman GF/F glass fiber filter (pore size of 0.7 µm) under low vacuum. The volume of the water sample was typically between 0.1 and 2 L to ensure that the absorptance of the particle-loaded filter did not exceed 0.4, as recommended by the IOCCG (International Ocean Color Coordination Group) Protocol [33]. The sample filters were stored at -80°C refrigerator until laboratory analysis. Briefly, the optical density (OD(λ)) of the sample filters between 250 and 800 nm was determined by a dual-beam PE Lambda 950 spectrophotometer equipped with an integrating sphere (150 mm in diameter) using the Transmittance-Reflectance (T-R) method [34,35], with the measured OD(λ) later converted to the spectral $a_p(\lambda)$ by accounting for the path-length amplification factor (β). Stepwise procedures for obtaining $a_p(\lambda)$, including the calculation of β, can be found in the latest IOCCG protocol [33]. $a_d(\lambda)$ were calculated from absorptance measurements on the same sample filters after pigment extraction with methanol, whereas $a_{ph}(\lambda)$ were simply calculated by subtracting $a_d(\lambda)$ from $a_p(\lambda)$.

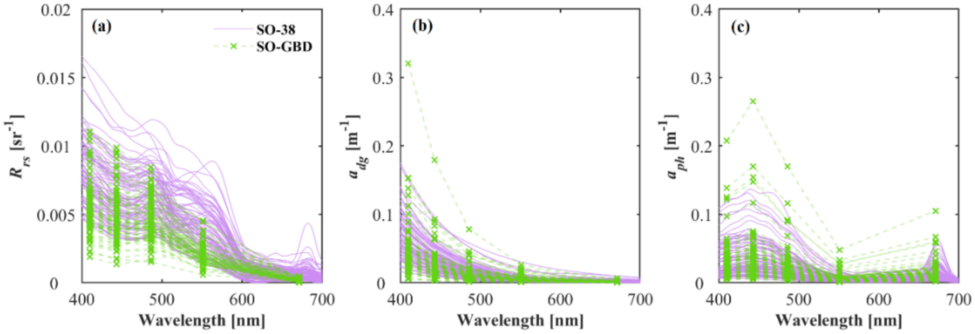

Fig. 2. Spectra of field-measured (a) $R_{rs}(\lambda)$, (b) $a_{dg}(\lambda)$, and (c) $a_{ph}(\lambda)$ from both SO-38 and SO-GBD datasets.

Measurements of $a_g(\lambda)$ were performed according to the IOCCG protocol [36]. Briefly, water samples were filtered through Millipore membranes (pore size of 0.2 µm) under a low vacuum immediately following collection. Sample filtrates were then collected in amber glass bottles and stored in the dark in a -20°C refrigerator during the cruise. The sample filtrates were unfrozen in a dark environment when returning to the laboratory, and the absorbance of the sample filtrates was measured using the same PE Lambda 950 spectrophotometer with a 10-cm cuvette, where Milli-Q water was used as the standard reference water blank.

Note that both $a_p(\lambda)$ and $a_g(\lambda)$ samples were prepared in duplicate during the cruise, and the final $a_p(\lambda)$ and $a_g(\lambda)$ were computed as an average of the duplicated samples after removing questionable spectra via visual inspection. In addition, a baseline correction was used to remove the residual scattering errors in the measured component absorption coefficients by subtracting the values of $a_p(750)$, $a_d(750)$, and $a_g(750)$ from the respective $a_p(\lambda)$, $a_d(\lambda)$ and $a_g(\lambda)$ spectra. Finally, the total absorption coefficient of seawater, $a(\lambda)$, was calculated as the sum of $a_p(\lambda)$, $a_g(\lambda)$, and the absorption coefficient of pure seawater, $a_w(\lambda)$. In this effort, $a_w(\lambda)$ values were taken from Pope and Fry [37] for 550 - 750 nm, but employed values of Lee et al. [38] for 350–550 nm, as the latter is closer to the 'true' absorption coefficient of pure seawater in the 350–550 nm domain [39]. In this effort, $a_w(\lambda)$ values are kept constant, although they vary slightly with temperature [40]. $a_{dg}(\lambda)$ were calculated as the sum of $a_d(\lambda)$ and $a_g(\lambda)$. In total, 72 concurrent measurements of $R_{rs}(\lambda)$ and the component absorption coefficients were obtained for SO-38.

Note that *in situ* measurements of $b_{bp}(\lambda)$ were absent in both SO-GBD and SO-38; therefore, we focused mainly on the evaluation of derived absorption coefficients by different water components. In general, the *in situ* data used for algorithm evaluation cover a variety of coastal and oceanic water regimes in the Southern Ocean with a wide range of different absorption properties (see Fig. 2(b) and 2(c)). For all measurements in the SO-GBD and SO-38, termed SO-All herein, $a_{nw}(443)$ (total absorption coefficient without pure seawater, in m^{-1}) ranged from 0.0084 to 0.31 m^{-1}, and the ratios of $a_{ph}(443)/a_{nw}(443)$ and $a_{dg}(443)/a_{nw}(443)$ varied in the range of 13.3% – 87.2% (51.8% ± 17.0%) and 12.8% – 86.7% (48.2% ± 17.0%), respectively, with the numbers in the brackets referring to the mean value and the standard deviation.

2.2. Satellite data

The standard Level-2 $R_{rs}(\lambda)$ products of Visible Infrared Imaging Radiometer Suite (VIIRS), downloaded from the NASA Ocean Color website (https://oceancolor.gsfc.nasa.gov), were employed in this study to perform the matchup analysis. VIIRS, onboard the Suomi National Polar-orbiting Partnership (SNPP) satellite, provides radiometric measurements, at a spatial resolution of 750 m, at six spectral bands in the visible domain centered at 410, 443, 486, 551, 671, and 745 nm, respectively. Note that the standard NASA Level-2 $R_{rs}(\lambda)$ was atmospherically corrected following the concept of the ‘black-pixel’ assumption in the near-infrared (NIR) bands [41], but using an iterative bio-optical modeling approach to accurately estimate the water-leaving radiance in the NIR bands [42]. In addition, $R_{rs}(\lambda)$ products of R2022.0 reprocessing were used in this effort.

Here, we computed the median value of all valid satellite-measured $R_{rs}(\lambda)$ from a 5-by-5-pixel box covering the *in situ* site as the matched VIIRS $R_{rs}(\lambda)$ measurements. Note that a strict comparison between satellite and *in situ* data usually requires a time difference of less than 3 h between the two measurements [43]. However, due to persistent cloud coverage and occasional sea ice appearance in our sampling locations, only a small number of matchups can be acquired under this strict criterion. Thus, the time difference was set to 24 hours in this effort to acquire matchups. Additionally, we used the QA score to assess the spectral quality of the VIIRS $R_{rs}(\lambda)$, and only $R_{rs}(\lambda)$ spectra with QA score ≥ 0.5 were retained. Note that radiometric measurements were not always concurrently collected with water sampling in SO-38, especially when some water samples were collected at night. In total, we obtained 24 matched measurements between VIIRS $R_{rs}(\lambda)$ and field-measured $R_{rs}(\lambda)$, and 35 matched measurements between VIIRS $R_{rs}(\lambda)$ and field-measured component absorption coefficients.

2.3. Semi-analytical algorithms

Two widely used SAAs, GIOP and QAA, were employed to evaluate their performance in the Southern Ocean. The GIOP model employs a quadratic expression to describe the relationship between the remote sensing reflectance just below the sea surface ($r_{rs}(\lambda)$) and IOPs (*i.e.*, $a(\lambda)$ and total backscattering coefficient $b_b(\lambda)$) [44]:

$$r_{rs}(\lambda) = \sum_{i=1}^{2} G_i \left[\frac{b_b(\lambda)}{a(\lambda)+b_b(\lambda)}\right]^i, \tag{2}$$

where G_1 and G_2 are constants that are spectrally fixed at 0.0949 and 0.0794 sr^{-1}, respectively. $r_{rs}(\lambda)$ can be converted from $R_{rs}(\lambda)$ as follows [23],

$$r_{rs}(\lambda) = \frac{R_{rs}(\lambda)}{0.52+1.7R_{rs}(\lambda)}. \tag{3}$$

In Eq. (2), $a(\lambda)$ can be calculated as the sum of all component absorption coefficients [45,46], and the absorption by each component can be expressed as a function of the eigenvector (mass-specific absorption spectrum, $a^*(\lambda)$) and eigenvalue (magnitude or concentration, M):

$$a(\lambda) = a_{\mathrm{w}}(\lambda) + M_{\mathrm{ph}}a^*_{\mathrm{ph}}(\lambda) + M_{\mathrm{d}}a^*_{\mathrm{d}}(\lambda) + M_{\mathrm{g}}a^*_{\mathrm{g}}(\lambda), \tag{4}$$

where the subscripts w, ph, d and g indicate the contribution of water, phytoplankton, non-algal particles (NAP) and CDOM, respectively. The eigenvectors $a^*_{\mathrm{d,g}}(\lambda)$ are denoted as exp($-S_{\mathrm{d,g}} \times (\lambda - 443)$), both $a^*_{\mathrm{d}}(\lambda)$ and $a^*_{\mathrm{g}}(\lambda)$ differ only in the exponential slopes, and thus the two components are typically combined for satellite applications and Eq. (4) becomes,

$$a(\lambda) = a_{\mathrm{w}}(\lambda) + M_{\mathrm{ph}}a^*_{\mathrm{ph}}(\lambda) + M_{\mathrm{dg}}a^*_{\mathrm{dg}}(\lambda). \tag{5}$$

Similar to $a(\lambda)$, $b_{\mathrm{b}}(\lambda)$ can be expressed as,

$$b_{\mathrm{b}}(\lambda) = b_{\mathrm{bw}}(\lambda) + M_{\mathrm{bp}}b^*_{\mathrm{bp}}(\lambda), \tag{6}$$

where subscripts w and p indicate the contribution of water molecules and particles, with the values of $b_{\mathrm{bw}}(\lambda)$ taken from Zhang et al. [47].

In this study, the default configuration of GIOP, referred to as GIOP for simplicity, was employed. Specifically, the eigenvector $a^*_{\mathrm{dg}}(\lambda)$ is denoted as exp($-S_{\mathrm{dg}} \times (\lambda - 443)$), where S_{dg} describes the spectral slope and is set to 0.018 nm^{-1}. The eigenvector $a^*_{\mathrm{ph}}(\lambda)$ was estimated using the approach described by Bricaud et al. [48] with remotely sensed Chla, and further with $a^*_{\mathrm{ph}}(443)$ forced as 0.055 $\mathrm{m}^2\ \mathrm{mg}^{-1}$ [19]. The band-ratio algorithm of OC3V was employed to estimate Chla from $R_{\mathrm{rs}}(\lambda)$ [49]. The eigenvector $b^*_{\mathrm{bp}}(\lambda)$ is expressed as $(551/\lambda)^{S\mathrm{bp}}$, where S_{bp} determines the steepness of the power-law variation in $b^*_{\mathrm{bp}}(\lambda)$ and is determined by the blue-to-green ratio of $R_{\mathrm{rs}}(\lambda)$ [23]. The eigenvalues, *i.e.*, M_{dg}, M_{ph}, and M_{bp}, were estimated from $R_{\mathrm{rs}}(\lambda)$ using spectral optimization with the Levenberg-Marquardt optimization. The component absorption and backscattering coefficients were subsequently derived from the eigenvalues and eigenvectors.

On the other hand, QAA algebraically solves IOPs from $R_{\mathrm{rs}}(\lambda)$ for optically deep water [23]. Here, the latest version (version 6) of the QAA, referred to as QAA herein for brevity, was used. Stepwise descriptions of QAA version 6 can be found at http://www.ioccg.org/groups/Software_OCA/QAA_v6_2014209.pdf. Briefly, QAA separates the inversion process into two consecutive parts. The first part involves the retrieval of $a(\lambda)$ and $b_{\mathrm{b}}(\lambda)$ from $R_{\mathrm{rs}}(\lambda)$. QAA initiates IOPs inversion with the empirical estimation of $a(\lambda)$ at a reference wavelength (*i.e.*, $a(\lambda_0)$, λ_0 stands for the reference wavelength), and then solves $b_{\mathrm{b}}(\lambda_0)$ algebraically from $R_{\mathrm{rs}}(\lambda_0)$ and $a(\lambda_0)$. Then, $b_{\mathrm{bp}}(\lambda_0)$ is calculated as the difference between $b_{\mathrm{b}}(\lambda_0)$ and $b_{\mathrm{bw}}(\lambda_0)$, and the spectral $b_{\mathrm{bp}}(\lambda)$ can be obtained from $b_{\mathrm{bp}}(\lambda_0)$ and the empirically-estimated S_{bp} following the power-law function. With known $b_{\mathrm{bp}}(\lambda)$, $b_{\mathrm{b}}(\lambda)$ can be obtained and, subsequently, the $a(\lambda)$. Note that the reference wavelength is set to 551 nm for relatively clear waters with $R_{\mathrm{rs}}(670)$ less than 0.0015 sr^{-1} and set to 670 nm for scenarios with $R_{\mathrm{rs}}(670)$ greater than 0.0015 sr^{-1}. In our compiled SO dataset, all $R_{\mathrm{rs}}(670)$ values were less than 0.0015 sr^{-1}. In the second part of the QAA, $a(\lambda)$ is partitioned into $a_{\mathrm{ph}}(\lambda)$ and $a_{\mathrm{dg}}(\lambda)$ algebraically after estimating the ratio of ζ and ξ, where ζ and ξ are the ratios of $a_{\mathrm{ph}}(410)/a_{\mathrm{ph}}(443)$ and $a_{\mathrm{dg}}(410)/a_{\mathrm{dg}}(443)$, respectively. Unlike GIOP treating S_{dg} as a constant, S_{dg} in QAA is a function of $r_{\mathrm{rs}}(443)/r_{\mathrm{rs}}(551)$. A simplified flow chart illustrating the inversion of IOPs by both GIOP and QAA can be found in Fig. 3.

Note that inelastic scattering processes, such as Raman scattering, could result in elevated $R_{\mathrm{rs}}(\lambda)$, particularly for the long wavelengths in oligotrophic waters. Therefore, prior to the implementation of both QAA and GIOP, a simple correction of $R_{\mathrm{rs}}(\lambda)$ for Raman scattering effects was performed following Lee et al. [50].

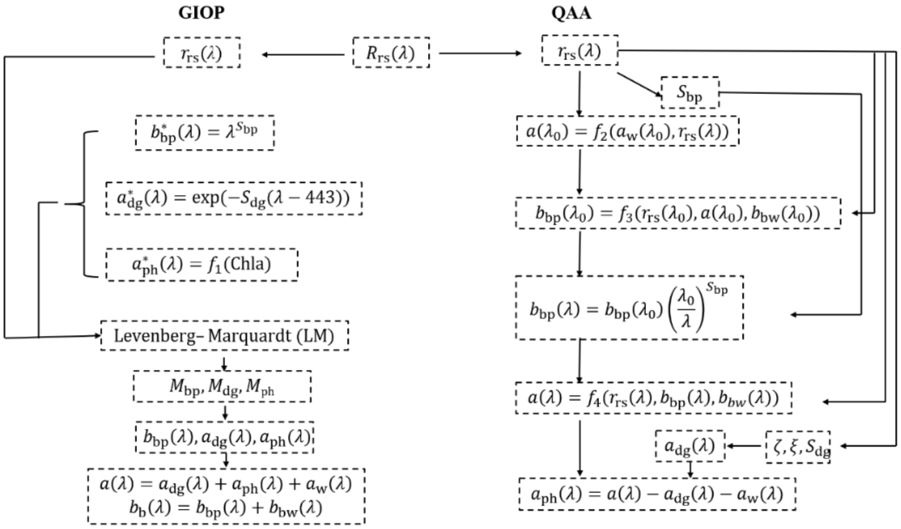

Fig. 3. Simplified flow chart illustrating GIOP and QAA for the inversion of IOPs.

2.4. Statistical metrics

The performances of both SAAs were quantified using statistical metrics calculated between derived IOPs and known values from *in situ* measurements, which included the median percentage difference (ε), Root Mean Square Difference (RMSD), Mean Absolute Percentage Difference (MAPD), and linear regression parameters, namely the slope and coefficient of determination (R^2). Linear regressions were performed on the logarithmically transformed IOPs. The first three metrics are defined as follows,

$$\varepsilon = \text{Median}\left(\frac{y_n}{x_n} - 1\right) \times 100\%, \tag{7}$$

$$\text{RMSD} = \sqrt{\frac{1}{\text{N}} \sum_{\text{n}=1}^{\text{N}} (y_n - x_n)^2}, \tag{8}$$

$$\text{MAPD} = \frac{1}{\text{N}} \sum_{\text{n}=1}^{\text{N}} \frac{|y_n - x_n|}{x_n} \times 100\%, \tag{9}$$

where x_n and y_n represent the known and derived IOPs, respectively, and N is the number of measurements used for metric calculation.

3. Results and discussion

3.1. Evaluation of derived IOPs from field-measured $R_{rs}(\lambda)$

The performance of both QAA and GIOP was first assessed using SO-38 and SO-GBD at the four VIIRS bands in the blue-green domain, *i.e.*, 410, 443, 486, and 551 nm. Here we only present the evaluation results of $a(\lambda)$, $a_{ph}(\lambda)$, and $a_{dg}(\lambda)$ derived by both SAAs. Retrieved IOPs at 670 nm are not necessary in this effort, as $a(670)$ is dominated by the absorption of pure seawater in our compiled dataset.

3.1.1. Evaluation of derived $a(\lambda)$ by both SAAs

We first evaluated the derived $a(\lambda)$ using the two SAAs, with scatterplots between the derived and measured $a(\lambda)$ presented in Fig. 4. The detailed statistical metrics used to quantify the performance of the two SAAs are listed in Table 1. To ensure consistency, the same $a_w(\lambda)$ values are employed in the inversion schemes as those used in the calculation of $a(\lambda)$ from the lab-measured component absorption coefficients.

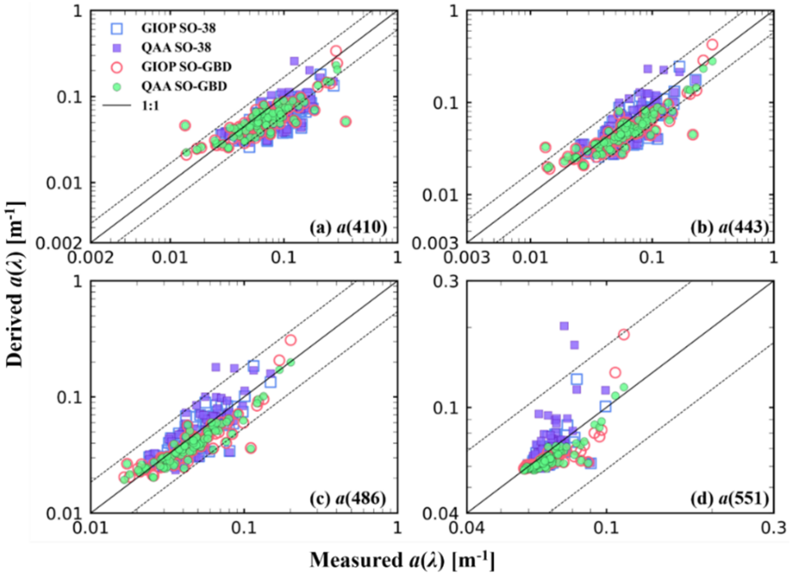

Fig. 4. Comparisons between *in situ* measured $a(\lambda)$ and that derived by QAA and GIOP at 410, 443, 486, and 551 nm, respectively. The solid black line indicates the 1:1 relationship, and the dashed lines represent the 1:1 line ± $20\%\log_{10}(\bar{a}(\lambda))$, with $\bar{a}(\lambda)$ as the mean $a(\lambda)$ of SO-All.

Table 1. Statistics of derived $a(\lambda)$ by both QAA and GIOP at 410, 443, 486, and 551 nm for SO-GBD, SO-38, and SO-All datasets, respectively

		QAA					GIOP				
		ε (%)	MAPD (%)	RMSD (m^{-1})	Slope	R^2	ε (%)	MAPD (%)	RMSD (m^{-1})	Slope	R^2
SO-GBD	$a(410)$	-21.5	28.0	0.047	0.58	0.68	-20.8	28.1	0.047	0.60	0.67
	$a(443)$	-20.8	25.8	0.032	0.70	0.78	-21.8	26.4	0.035	0.72	0.76
	$a(486)$	-14.0	17.8	0.015	0.78	0.82	-13.8	18.6	0.020	0.80	0.80
	$a(551)$	-6.1	7.0	0.007	0.84	0.78	-5.3	8.0	0.011	0.94	0.62
SO-38	$a(410)$	-30.1	34.7	0.047	0.68	0.46	-36.3	35.5	0.048	0.61	0.51
	$a(443)$	-10.5	28.4	0.033	0.86	0.57	-14.7	24.8	0.026	0.81	0.62
	$a(486)$	3.4	25.3	0.024	1.00	0.62	-3.5	19.3	0.016	0.87	0.66
	$a(551)$	0.0	12.5	0.021	1.44	0.37	-2.9	6.4	0.008	0.90	0.46
SO-All	$a(410)$	-27.0	31.1	0.047	0.60	0.58	-28.1	31.5	0.047	0.58	0.60
	$a(443)$	-17.5	27.0	0.032	0.76	0.67	-20.0	25.7	0.031	0.75	0.70
	$a(486)$	-8.8	21.3	0.019	0.87	0.69	-11.1	18.9	0.018	0.84	0.73
	$a(551)$	-4.0	9.5	0.015	1.00	0.39	-4.7	7.3	0.010	0.92	0.55

As shown in Fig. 4, retrieved $a(\lambda)$ by both GIOP and QAA show good agreement with the measured $a(\lambda)$. Overall, the MAPD values of $a(\lambda)$ from both algorithms ranged from ~8% at 551 nm to ~31% at 410 nm, with remotely sensed $a(\lambda)$ slightly lower than that from the water samples (see Table 1 for details). This is equivalent to those reported in the literature [18,19,51], but better than those reported in coastal regions such as the South China Sea [52]. A larger deviation of $a(\lambda)$ at the shorter wavelengths was also observed in the high-latitude Arctic region [51], and there are a few reasons behind this pattern. First, the statistically good performance at 551 nm is largely attributed to the fact that $a_w(\lambda)$ is the dominant component of $a(\lambda)$ at 551 nm for SO-All ($a_w(551)/a(551) \sim 0.83$). For the blue bands, on the one hand, there is an impact associated with the empirically estimated S_{bp}. As both QAA and GIOP assume the same spectral shape of $b_{bp}(\lambda)$, uncertainties in S_{bp} could be propagated to the estimated $b_{bp}(\lambda)$, and such impacts would be amplified for $b_{bp}(\lambda)$ at shorter wavelengths [53,54], which will subsequently affect the analytical inversion of $a(\lambda)$ from $R_{rs}(\lambda)$. For instance, S_{bp} for waters in SO is generally between 1 and 2 [55], if S_{bp} changes from 1.5 to 1.8 (increased by 20%), derived $b_{bp}(410)$ will be elevated by 9.3%, in comparison to a 3.8% increasing of derived $b_{bp}(486)$. This is particularly important as the empirically estimated S_{bp} from the band ratio of $R_{rs}(\lambda)$ could have relatively large uncertainties [54,55]. On the other hand, field-measured $a(\lambda)$ could have relatively larger measurement errors in blue bands than in green bands. For instance, the residual scattering errors of lab-measured $a_p(\lambda)$ and $a_g(\lambda)$ typically decrease towards longer wavelengths, and the baseline correction approach may not be able to fully correct these errors in the blue bands [56].

Based on the metrics shown in Table 1, for the respective dataset of SO-GBD and SO-38, QAA and GIOP have overall similar performance in retrieving $a(\lambda)$, as indicated by the values of ε and MAPD. However, between the two algorithms, QAA performed slightly better in SO-GBD in terms of RMSD and R^2, while GIOP predicted overall more accurate $a(\lambda)$ in SO-38. Across different datasets, it appears that the uncertainties of $a(\lambda)$ by both SAAs are relatively smaller for SO-GBD than for SO-38. For example, larger uncertainties of $a(410)$ by both SAAs were observed in SO-38, with greater ε values in SO-38 (ε = -30.2% and -37.4% for QAA and GIOP, respectively) than that in SO-GBD (ε = -21.5% and -20.8%). These results suggest that there could be slightly larger uncertainties in SO-38 than in SO-GBD, either in the measured $R_{rs}(\lambda)$, $a(\lambda)$, or both. As discussed in previous studies, the above-water approach does not provide a direct measurement of $L_w(\lambda)$, and it is quite challenging to adequately remove the surface-reflected light when the sea surface is roughened by waves, especially in the Southern Ocean, where the reflected light consists of glints from sky, sun, and broken-ice [30,57–59]. Nevertheless, the MAPD and ε values shown in this study were within the range observed in the algorithm evaluation reported in the literature [19,52].

3.1.2. Evaluation of derived $a_{ph}(\lambda)$ by both SAAs

Following the same evaluation strategy for derived $a(\lambda)$, we further compared the derived $a_{ph}(\lambda)$ by GIOP and QAA with the measured $a_{ph}(\lambda)$, with results presented in Fig. 5. Detailed statistical metrics are given in Table 2.

As shown in Fig. 5, derived $a_{ph}(\lambda)$ by both SAAs agree well with measured values at the four wavelengths, where nearly all points are well distributed along the 1:1 line, suggesting that both GIOP and QAA provide satisfying $a_{ph}(\lambda)$ retrievals for the compiled dataset. In general, GIOP and QAA have quite comparable performances in predicting $a_{ph}(\lambda)$ in SO-All. Statistically, GIOP slightly outperforms QAA in terms of MAPD, where the MAPD of the GIOP-derived $a_{ph}(\lambda)$ ranges between 35.8% and 40.9% for 410–486 nm, which is ~10% smaller than that of QAA-derived $a_{ph}(\lambda)$. However, QAA could be deemed to perform better in terms of ε and RMSD (see metrics in Table 2). These metrics are quite consistent with the evaluation results of both SAAs using measurements from the South China Sea and the IOCCG dataset, where MAPD of derived $a_{ph}(\lambda)$ in the blue bands ranges from 25% to 60% [19,52]. Relatively larger uncertainties were observed at $a_{ph}(551)$ by both SAAs with MAPD of 123.0% and 56.8% for retrievals from QAA and GIOP, respectively. This large deviation in derived $a_{ph}(551)$ is mainly because $a_{ph}(551)$ values are very small for these waters ($a_{ph}(551)$ only accounts for ~ 8% of $a(551)$). Thus, the

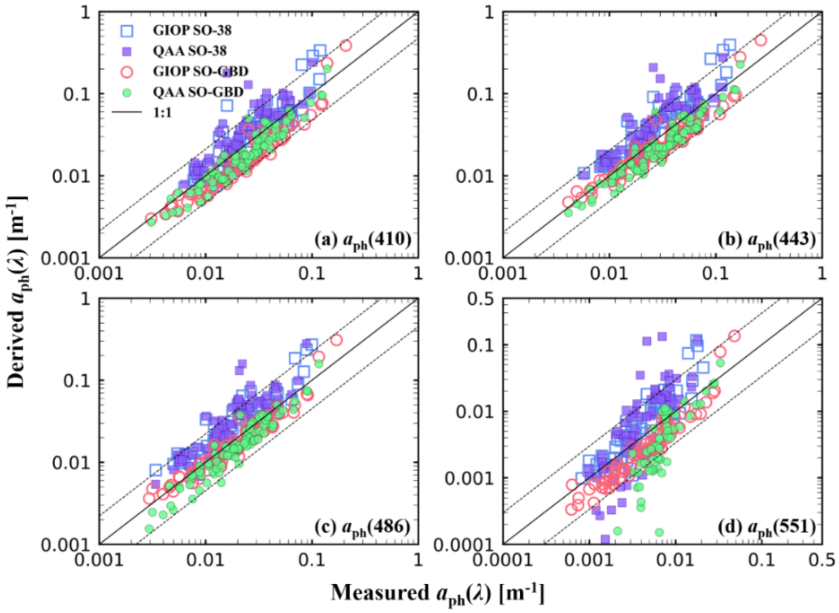

Fig. 5. Same as Fig. 4, but for derived $a_{ph}(\lambda)$.

Table 2. Same as Table 1, but for derived $a_{ph}(\lambda)$

		QAA					GIOP				
		ε (%)	MAPD (%)	RMSD (m^{-1})	Slope	R^2	ε (%)	MAPD (%)	RMSD (m^{-1})	Slope	R^2
SO-GBD	$a_{ph}(410)$	-25.3	26.7	0.013	1.00	0.91	-34.3	33.4	0.027	0.98	0.91
	$a_{ph}(443)$	-23.7	25.7	0.015	0.97	0.91	-25.4	25.8	0.028	0.92	0.90
	$a_{ph}(486)$	-21.6	24.5	0.008	1.07	0.92	-16.1	20.1	0.019	0.94	0.92
	$a_{ph}(551)$	-49.0	51.7	0.004	2.09	0.71	-43.3	42.3	0.011	1.13	0.91
SO-38	$a_{ph}(410)$	32.9	67.6	0.034	0.99	0.69	13.2	38.5	0.040	1.06	0.81
	$a_{ph}(443)$	56.9	75.0	0.040	0.97	0.72	46.0	55.6	0.049	0.99	0.82
	$a_{ph}(486)$	67.4	85.2	0.036	1.02	0.74	53.3	64.7	0.033	0.95	0.83
	$a_{ph}(551)$	81.3	181.7	0.025	1.75	0.66	37.4	73.2	0.017	1.28	0.81
SO-All	$a_{ph}(410)$	-8.2	45.5	0.025	1.00	0.72	-16.7	35.8	0.033	1.02	0.79
	$a_{ph}(443)$	-3.2	48.4	0.030	0.94	0.69	-1.4	39.7	0.039	0.93	0.76
	$a_{ph}(486)$	-1.1	52.5	0.025	1.03	0.70	4.6	40.9	0.027	0.94	0.78
	$a_{ph}(551)$	-3.9	123.0	0.019	1.37	0.40	-18.8	56.8	0.014	1.15	0.73

retrieval of $a_{ph}(551)$ is highly sensitive to errors in the derived $a(551)$, which is particularly true for QAA-derived $a_{ph}(\lambda)$, where $a_{ph}(551)$ is solely derived from $a(551)$. In particular, $a_{ph}(551)$ derived by QAA could even be negative for waters with very low $a_{ph}(551)$. For GIOP-derived $a_{ph}(551)$, it is an extension of the estimated $a_{ph}(443)$ based on the pre-assumed $a_{ph}(\lambda)$ spectral shape; thus, it is not highly dependent on the value of $a(551)$. For SO-All, QAA yielded a few negative $a_{ph}(551)$ retrievals ($N = 28$), as also observed in Arctic and low-latitude waters [51]. Those negative retrievals were removed from further statistical analysis. Consequently, there were fewer scatter points from QAA-derived $a_{ph}(551)$ in Fig. 5(d) compared to those from GIOP.

However, negative $a_{\text{ph}}(551)$ retrievals could be easily recovered by linking $a_{\text{ph}}(551)$ with $a_{\text{ph}}(443)$ if needed [19,21].

Between SO-GBD and SO-38, it appears that both SAAs present better agreement in $a_{\text{ph}}(\lambda)$ for SO-GBD. Statistically, retrieved $a_{\text{ph}}(\lambda)$ by both SAAs showed overall higher values of ε, MAPD, RMSD, and slope, and smaller R^2 in SO-38 compared to that in SO-GBD. Generally, ε is greater than 0 for both SAAs for SO-38, indicating that the retrievals from these algorithms are higher than *in situ* measurements for SO-38, but the opposite is true for SO-GBD.

3.1.3. Evaluation of derived $a_{\text{dg}}(\lambda)$ by both SAAs

A comparison between the derived $a_{\text{dg}}(\lambda)$ by both SAAs and *in situ* $a_{\text{dg}}(\lambda)$ is presented in Fig. 6, with the statistical measures tabulated in Table 3. Compared to the generally quite consistent retrievals of $a_{\text{ph}}(\lambda)$ and $a(\lambda)$, derived $a_{\text{dg}}(\lambda)$ from both SAAs showed large deviations versus *in situ* measurements for both SO-38 and SO-GBD. Specifically, at the lower end ($a_{\text{dg}}(443) < \sim 0.01$ m^{-1}), $a_{\text{dg}}(\lambda)$ from SAAs are systematically higher, but $a_{\text{dg}}(\lambda)$ from SAAs are lower at the higher end ($a_{\text{dg}}(443) > \sim 0.03$ m^{-1}). As a result, while *in situ* $a_{\text{dg}}(443)$ shows a range of ~0.003 to 0.2 m^{-1}, $a_{\text{dg}}(443)$ from $R_{\text{rs}}(\lambda)$ is in the range of ~0.003 to 0.03 m^{-1}, *i.e.*, a much narrower dynamic range from remote sensing. In particular, there are a few stations where $a_{\text{dg}}(443)$ from $R_{\text{rs}}(\lambda)$ is ~10 times lower than *in situ*-measured $a_{\text{dg}}(443)$. This result is quite puzzling as very good agreements are observed for $a(\lambda)$ and $a_{\text{ph}}(\lambda)$ (see Fig. 4 and Fig. 5), especially *in situ* $a(\lambda)$ is simply a sum of $a_{\text{w}}(\lambda)$, $a_{\text{ph}}(\lambda)$, and $a_{\text{dg}}(\lambda)$, and the dynamic ranges for both of $a_{\text{ph}}(\lambda)$ and $a_{\text{dg}}(\lambda)$ in SO-All are similar (*i.e.*, $a_{\text{ph}}(\lambda)$ is not dominating $a(\lambda)$). In the following, we try to provide a thorough explanation of this deviation.

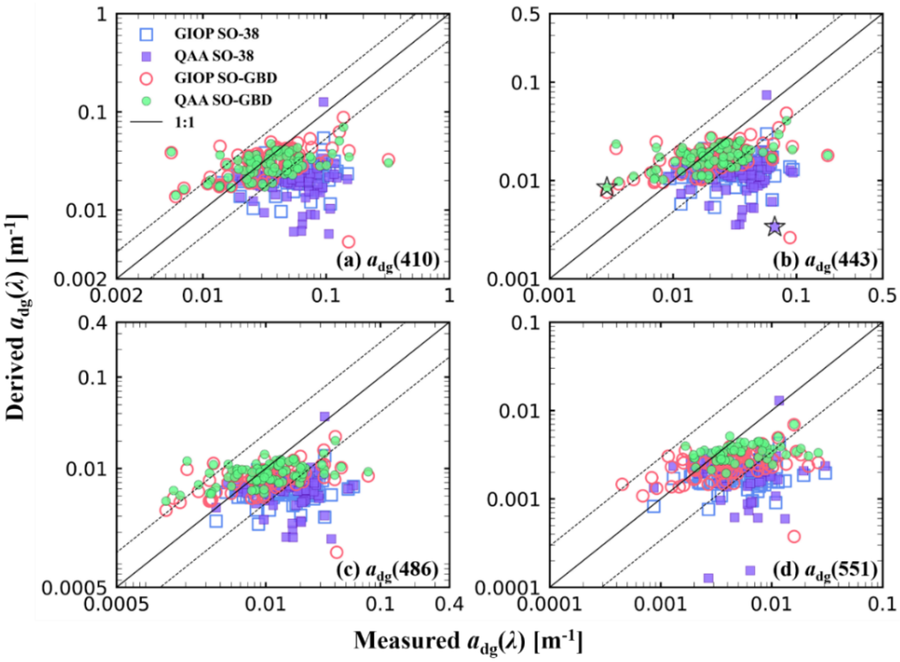

Fig. 6. Same as Fig. 4, but for derived $a_{\text{dg}}(\lambda)$.

As illustrated clearly with the QAA scheme, while the retrieval of $a(\lambda)$ is governed by the spectral shape of $R_{\text{rs}}(\lambda)$, the separation of $a_{\text{ph}}(\lambda)$ and $a_{\text{dg}}(\lambda)$ from $a(\lambda)$ is determined by $a(\lambda)$ in the blue bands and the spectral shapes of $a_{\text{ph}}(\lambda)$ and $a_{\text{dg}}(\lambda)$, *i.e.*, the ζ ($a_{\text{ph}}(410)/a_{\text{ph}}(443)$) and ξ ($a_{\text{dg}}(410)/a_{\text{dg}}(443)$) parameters. Generally, ζ is within a narrow range, so it does not

Table 3. Same as Table 1, but for derived $a_{dg}(\lambda)$

		QAA					GIOP				
		ε (%)	MAPD (%)	RMSD (m^{-1})	Slope	R^2	ε (%)	MAPD (%)	RMSD (m^{-1})	Slope	R^2
SO-GBD	$a_{dg}(410)$	-19.1	46.8	0.045	0.07	0.01	-12.7	45.6	0.043	0.17	0.11
	$a_{dg}(443)$	-18.7	52.2	0.026	0.07	0.01	-16.9	49.0	0.026	0.17	0.12
	$a_{dg}(486)$	-16.1	57.5	0.013	0.07	0.01	-23.4	51.1	0.013	0.17	0.13
	$a_{dg}(551)$	-29.3	42.6	0.006	-0.05	0.00	-39.9	50.6	0.006	0.17	0.13
SO-38	$a_{dg}(410)$	-65.1	62.1	0.051	0.04	0.00	-61.0	55.7	0.047	0.12	0.04
	$a_{dg}(443)$	-66.3	59.8	0.030	0.03	0.00	-62.5	56.0	0.029	0.11	0.04
	$a_{dg}(486)$	-64.9	58.0	0.016	0.05	0.00	-63.6	57.5	0.016	0.10	0.04
	$a_{dg}(551)$	-61.9	57.8	0.006	0.03	0.00	-66.5	59.9	0.006	0.08	0.03
SO-All	$a_{dg}(410)$	-43.9	53.8	0.048	-0.07	0.01	-37.7	50.2	0.045	0.06	0.01
	$a_{dg}(443)$	-41.5	55.6	0.028	-0.05	0.00	-41.4	52.1	0.027	0.07	0.02
	$a_{dg}(486)$	-37.1	57.7	0.014	-0.04	0.00	-44.0	54.0	0.014	0.08	0.02
	$a_{dg}(551)$	-49.7	50.9	0.006	0.01	0.00	-52.9	54.8	0.006	0.11	0.04

significantly impact the derivation of $a_{ph}(\lambda)$ and $a_{dg}(\lambda)$. For instance, if the value of ζ increases by 10%, the QAA-derived $a_{dg}(443)$ will be changed by less than $\sim$2%.On the other hand, ξ, equivalent to exp(S_{dg}(443-410)), could change from 1.39 ($S_{dg} = 0.01$ nm^{-1}) to 1.93 ($S_{dg} = 0.02$ nm^{-1}), and higher S_{dg} value will result in lower $a_{dg}(443)$. Therefore, if *in situ* data are assumed to be accurate, to balance the higher retrieval at the lower end and lower retrieval at the higher end, as shown in Fig. 6, it requires a higher S_{dg} value at the lower end, while a lower S_{dg} value at the higher end, rather than a nearly fixed S_{dg} value ($\sim$0.016 nm^{-1} for QAA and 0.018 nm^{-1} for GIOP) in both SAAs. Such a spatial variation of S_{dg} is not yet known in the SO and has not been reported in the literature for other regions. Furthermore, a 100% increase of S_{dg} from 0.01 to 0.02 nm^{-1} will only result in $a_{dg}(410)$ increasing by $\sim$39% and $a_{dg}(551)$ declining by $\sim$66%. In short, errors in estimated ζ and ξ could not be the primary sources to explain the large deviations observed in derived $a_{dg}(\lambda)$.

This is further supported by evaluations of both SAAs with GBD-Global, where Fig. 7 compares the derived $a_{dg}(443)$ with the measured values. For this more inclusive dataset, we do not observe the "twisted" pattern as shown in Fig. 6. Statistically, the slope and R^2 values between the estimated and measured log($a_{dg}(443)$) are close to 1.0, which are significantly better than those of the SO datasets. Moreover, as shown in Fig. 7, the points of the SO dataset generally overlap with those of the GBD-Global, indicating that the quality of the SO dataset is overall equivalent to that of the global dataset, or at least no significant regional bias. These comparisons further indicate that the nearly constant S_{dg} values used in both SAAs are in general acceptable for the retrieval of a_{dg}.

The "twisted" pattern shown in Fig. 7 is more likely due to the inconsistency between measured $R_{rs}(\lambda)$ and measured $a_{dg}(\lambda)$ in the blue bands, as revealed between measured $R_{rs}(\lambda)$ and modeled $R_{rs}(\lambda)$ using measured IOPs (see Fig. 8). For example, for a station where the estimated $a_{dg}(\lambda)$ is much lower than the measured $a_{dg}(\lambda)$ (the higher end as shown in Fig. 6(b)), Fig. 8(a) shows the comparison between measured $R_{rs}(\lambda)$ and modeled $R_{rs}(\lambda)$, where the latter one was simulated used *in situ* $a(\lambda)$ along with an optimized $b_b(\lambda)$ for the best match in the green-red wavelengths following Eqs. (2) – (3). In this case, the $R_{rs}(410)/R_{rs}(443)$ ratio of the modeled $R_{rs}(\lambda)$ is $\sim$0.9, but this ratio from the measured $R_{rs}(\lambda)$ is $\sim$1.4, *i.e.*, measured R_{rs}(blue) is significantly higher than modeled R_{rs}(blue). Since blue bands play the major role in the retrieval of $a_{dg}(\lambda)$ and $R_{rs}(\lambda)$ is an inverse function of $a(\lambda)$, this no closure in R_{rs}(blue) caused $a_{dg}(\lambda)$ derived from

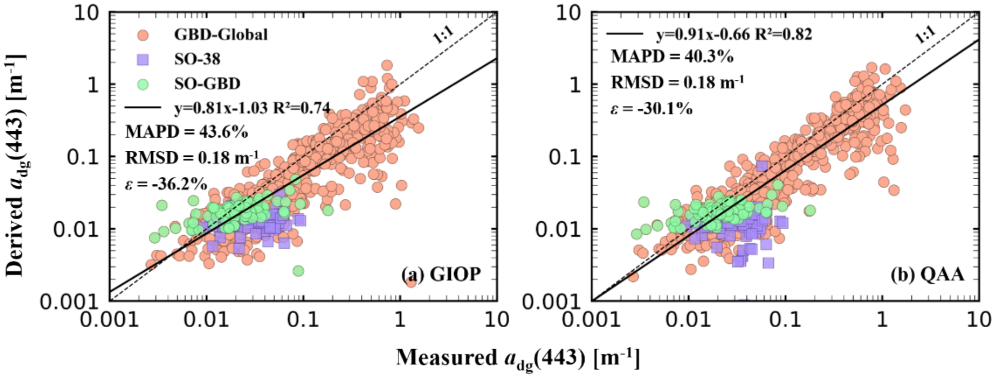

Fig. 7. Comparisons between measured $a_{\mathrm{dg}}(443)$ and that derived by (a) GIOP and (b) QAA for measurements from GBD-Global (tan circles), SO-38 (purple squares), and SO-GBD (green circles) datasets. The solid black line indicates the regression line for all data and the dashed line for the 1:1 relationship.

the two SAAs much lower than measured $a_{\mathrm{dg}}(\lambda)$. Conversely, for the case at the lower end of $a_{\mathrm{dg}}(\lambda)$ as shown in Fig. 6(b), the simulated $R_{\mathrm{rs}}(\lambda)$ with known $a(\lambda)$ is much higher than the measured $R_{\mathrm{rs}}(\lambda)$ in the blue bands (see Fig. 8(b)), *i.e.*, retrieved $a_{\mathrm{dg}}(\lambda)$ is higher than measured $a_{\mathrm{dg}}(\lambda)$ due to this no closure. Possible sources of errors or uncertainties for the no closure in R_{rs}(blue) include insufficient corrections of the residual scattering for measured $a_{\mathrm{dg}}(\lambda)$ [33,36] and incomplete removal of surface-reflected skylight for the measurement of $R_{\mathrm{rs}}(\lambda)$ [58], where both could significantly impact $a_{\mathrm{dg}}(\lambda)$ or $R_{\mathrm{rs}}(\lambda)$ in the blue bands. Nevertheless, Fig. 8 suggests that optical closure between measured IOPs and $R_{\mathrm{rs}}(\lambda)$ can be reached for the 450–700 nm domain, which supports the overall good agreement observed between measured and retrieved $a(\lambda)$ and $a_{\mathrm{ph}}(\lambda)$. Further, due to that $a_{\mathrm{dg}}(\lambda)$ is just one component of the total absorption coefficient, the relative impact of $a_{\mathrm{dg}}(\lambda)$ is different between the evaluation of $a_{\mathrm{dg}}(\lambda)$ and the evaluation of $a(\lambda)$. For instance, the ratio of $a_{\mathrm{dg}}(443)$ to $a(443)$ is ~0.42 ± 0.16 (significantly lower for longer wavelengths) for SO-All, i.e., any deviations in $a_{\mathrm{dg}}(443)$ will be about halved for deviations in $a(443)$, which is consistent with the observations shown in Fig. 4 where overall better agreements are found in the longer wavelengths.

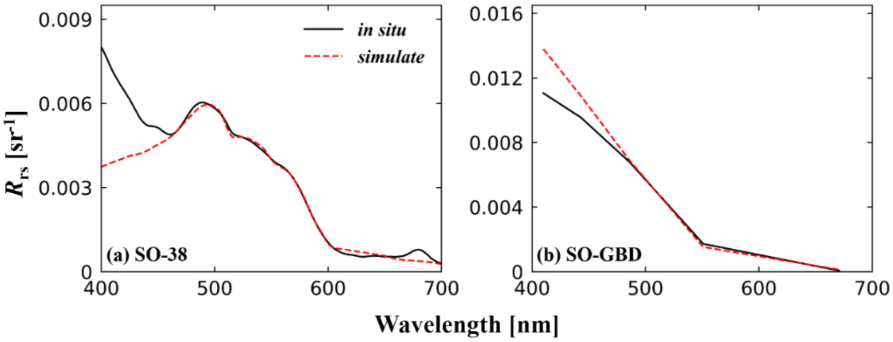

Fig. 8. Examples of measured $R_{\mathrm{rs}}(\lambda)$ compared with simulated $R_{\mathrm{rs}}(\lambda)$ using measured IOPs. (a) for a station with measured $a_{\mathrm{dg}}(\lambda)$ in the higher end (the black star shown in Fig. 6(b)), while (b) for a station with measured $a_{\mathrm{dg}}(\lambda)$ in the lower end (also a black star shown in Fig. 6(b)). The solid black line represents measured $R_{\mathrm{rs}}(\lambda)$, while the red dashed line for simulated $R_{\mathrm{rs}}(\lambda)$.

In addition, the retrieval of $a_{\text{ph}}(\lambda)$ by SAAs is primarily determined by $R_{\text{rs}}(\lambda)$ at blue-green bands (*i.e.*, 443 and 551 nm), while $a_{\text{dg}}(\lambda)$ is largely determined by $R_{\text{rs}}(\lambda)$ at blue bands (*i.e.*, 410 and 443 nm). Thus, failure or no closure at the blue bands has relatively small impacts on the retrieval of $a_{\text{ph}}(\lambda)$. In other words, the performance of both SAAs in retrieving $a_{\text{dg}}(\lambda)$ is largely dependent on the accuracy of measured $R_{\text{rs}}(\lambda)$ at blue bands, which highlights the importance of accurate atmospheric correction for the global estimation of $a_{\text{dg}}(\lambda)$. On the other hand, as long as ocean color satellites can provide good $R_{\text{rs}}(\lambda)$ products at 443 and 551 nm, small errors in $R_{\text{rs}}(410)$ may not significantly affect the retrieval of $a_{\text{ph}}(\lambda)$ by SAAs.

3.2. Evaluation of VIIRS $R_{rs}(\lambda)$ and IOPs products

Since the ultimate objective of the IOPs inverse algorithm is to obtain the spatial-temporal distribution of IOPs in the global ocean, it is of great interest to evaluate the derived IOPs by both SAAs from satellite measurements. In this effort, VIIRS matchups, with the locations of satellite-*in situ* matchups shown in Fig. 1, were employed for the evaluation.

3.2.1. Evaluation of VIIRS-measured $R_{\text{rs}}(\lambda)$

The robustness of satellite-derived IOPs is, of the first order, determined by the accuracy of the atmospherically corrected $R_{\text{rs}}(\lambda)$ from satellite measurements. Thus, we first evaluated the quality of the standard VIIRS $R_{\text{rs}}(\lambda)$ product for the Southern Ocean. Specifically, VIIRS $R_{\text{rs}}(\lambda)$ at 410, 443, 486, and 551 nm were evaluated against matched field-measured $R_{\text{rs}}(\lambda)$ from the SO-38 dataset (N = 24) (see Fig. 9). Note that only good-quality VIIRS-$R_{\text{rs}}(\lambda)$ (QA score ≥ 0.5) were employed for the matchup analysis.

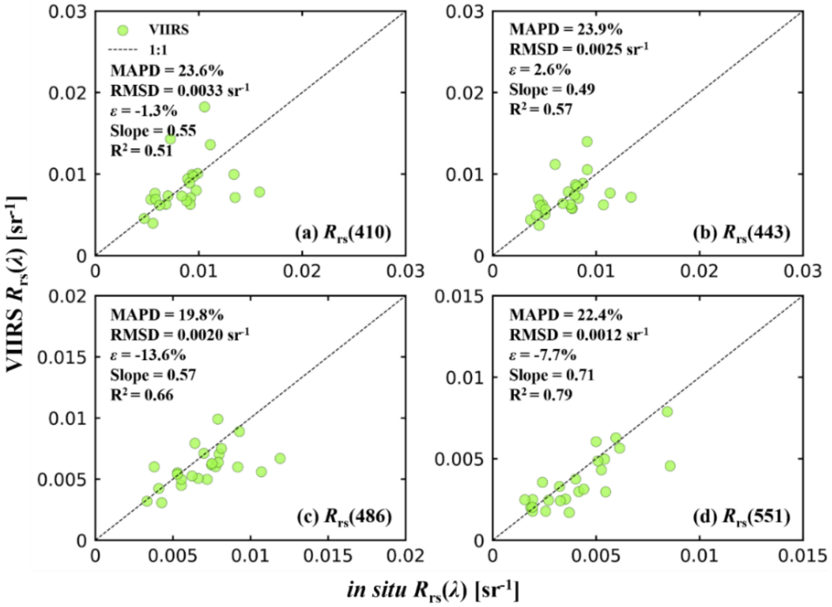

Fig. 9. Comparisons between VIIRS-measured and matched *in situ*-measured $R_{\text{rs}}(\lambda)$ at (a) 410 nm, (b) 443 nm, (c) 486 nm, and (d) 551 nm, respectively.

VIIRS-measured $R_{\text{rs}}(\lambda)$ agree overall well with *in-situ* $R_{\text{rs}}(\lambda)$ at the four VIIRS bands with MAPD values ranging between 19.8% and 23.9%, and there are no systematic deviations between VIIRS and *in situ* $R_{\text{rs}}(\lambda)$ at these bands (ε in a range of -1.3 – -13.6%). Slightly larger uncertainties were observed at the two blue bands in terms of MAPD and R^2, which could be probably due to uncertainties associated with the atmospheric correction for blue wavelengths [60]. Note that the error statistics of VIIRS-measured $R_{rs}(\lambda)$ in this effort are overall consistent with previous studies on the evaluation of VIIRS $R_{rs}(\lambda)$ [61–63], and the cross-sensor validations [64–66]. Thus, it is feasible to use the standard VIIRS $R_{rs}(\lambda)$ product screened by the QA score to generate confident IOPs products in the Southern Ocean.

3.2.2. Evaluation of VIIRS-derived IOPs

Both GIOP and QAA were applied to VIIRS $R_{rs}(\lambda)$ and the derived IOPs at 410, 443, and 486 nm were then compared with the matched field-measured $a(\lambda)$, $a_{dg}(\lambda)$, and $a_{ph}(\lambda)$ (see Fig. 10), with detailed statistical metrics provided in Table 4. In general, as found with field-measured $R_{rs}(\lambda)$, both SAAs have quite comparable performance in the retrieval of absorption coefficients by different water components. Moreover, uncertainties in VIIRS-derived $a(\lambda)$ and $a_{ph}(\lambda)$ by both SAAs are overall smaller than that of derived $a_{dg}(\lambda)$, which are also consistent with results obtained from filed measured $R_{rs}(\lambda)$. Statistically, MAPD of derived $a(\lambda)$ and $a_{ph}(\lambda)$ by both SAAs are ~30% and ~40%, respectively, in comparison to MAPD of ~60% for derived $a_{dg}(\lambda)$. In particular, $a_{ph}(\lambda)$ from VIIRS by both SAAs explained more than ~70% of the variability ($R^2 > 0.7$), providing confidence to use VIIRS-derived $a_{ph}(\lambda)$ for further applications, such as the estimation of chlorophyll concentration [48,67] or primary production [7,8]. For $a_{dg}(\lambda)$, however, there is also a "twisted" pattern between the retrieved and measured values, which is reflected in the very small slope and R^2 values. As indicated in the above section, this pattern is a puzzle, as it was shown in both SO-38 and SO-GBD, which is probably due to uncertainties in $a_{dg}(\lambda)$ measurements and the inversion algorithms (*i.e.*, S_{dg} in GIOP, ζ and ξ in QAA).

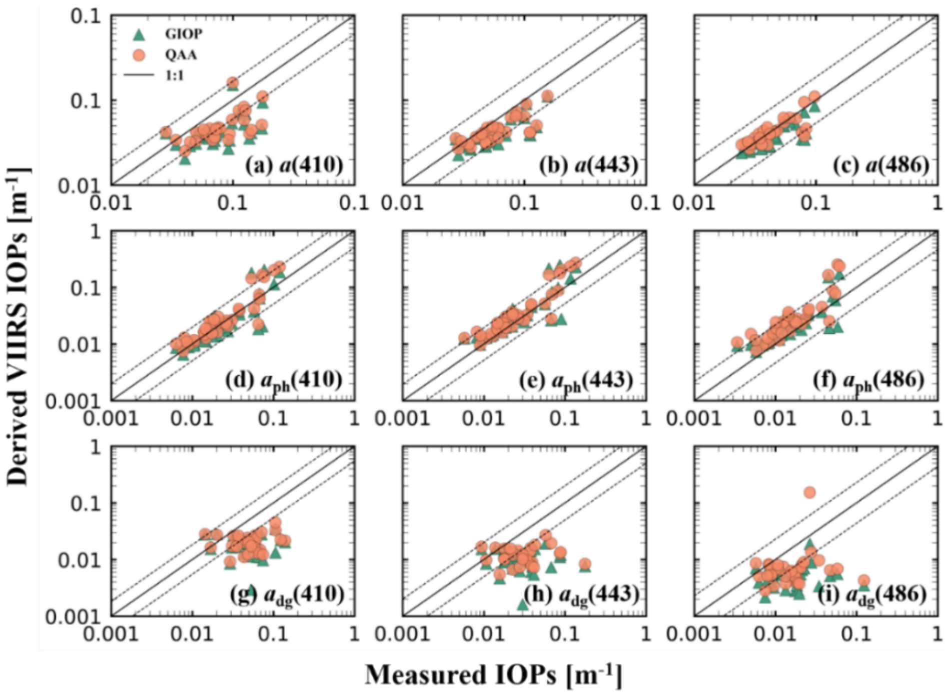

Fig. 10. Evaluation of VIIRS-derived IOPs by GIOP and QAA using the matchups. The upper, middle, and lower panels show the results for derived $a(\lambda)$, $a_{ph}(\lambda)$, and $a_{dg}(\lambda)$, respectively. The orange circles and green triangles represent the results of QAA and GIOP, respectively. The solid black line indicates the 1:1 relationship and the dashed lines represent the 1:1 line ± 20% $\log_{10}(\overline{\text{IOPs}})$, with $\overline{\text{IOPs}}$ as the mean value of matched *in situ* IOPs.

Table 4. Statistics of derived $a(\lambda)$, $a_{ph}(\lambda)$, and $a_{dg}(\lambda)$ from VIIRS matchups by both QAA and GIOP at 410, 443, and 486 nm, respectively

	QAA					GIOP				
	ε (%)	MAPD (%)	RMSD (m^{-1})	Slope	R^2	ε (%)	MAPD (%)	RMSD (m^{-1})	Slope	R^2
$a(410)$	-45.6	46.9	0.053	0.48	0.31	-37.5	41.9	0.049	0.51	0.36
$a(443)$	-24.9	29.1	0.030	0.61	0.59	-23.2	25.6	0.029	0.58	0.60
$a(486)$	-11.8	17.4	0.016	0.62	0.60	0.2	15.7	0.014	0.69	0.61
$a_{ph}(410)$	-4.6	32.2	0.035	0.99	0.74	11.6	35.7	0.037	1.05	0.83
$a_{ph}(443)$	19.4	42.1	0.043	0.91	0.74	23.8	44.6	0.044	1.01	0.84
$a_{ph}(486)$	30.9	53.0	0.029	0.80	0.68	58.9	88.6	0.052	0.99	0.76
$a_{dg}(410)$	-65.0	63.9	0.048	-0.06	0.00	-60.8	60.3	0.046	0.09	0.02
$a_{dg}(443)$	-67.5	64.6	0.043	-0.04	0.00	-62.3	59.3	0.042	0.04	0.00
$a_{dg}(486)$	-68.8	64.4	0.027	0.06	0.01	-61.5	70.1	0.035	0.17	0.03

The statistical measures for derived $a(\lambda)$ and $a_{ph}(\lambda)$ from VIIRS-measured $R_{rs}(\lambda)$ are overall worse than those from field-measured $R_{rs}(\lambda)$, which could be expected because errors in the atmospherically-corrected $R_{rs}(\lambda)$ will inevitably propagate to the derived IOPs, especially for the short blue bands [60]. In addition, the mismatch between satellite and field measurements due to the time and space gap will also introduce deviations between satellite and field measurements [68–70], especially when we employed a relatively relaxed time window (*i.e.*, 24h) to acquire satellite-field matchups (see Section 2.2). Nevertheless, from the evaluations of both satellite and field measurements, we can conclude that QAA and GIOP can derive overall satisfying retrievals of $a(\lambda)$ and $a_{ph}(\lambda)$ in the Southern Ocean, with MAPD of derived $a(\lambda)$ and $a_{ph}(\lambda)$ being ~20% and ~40%, respectively. However, large uncertainties are observed in derived $a_{dg}(\lambda)$ (MAPD > 60%), and it may require more high-quality field data and regional optimized inversion algorithms to resolve the puzzle associated with the "twisted" pattern about $a_{dg}(\lambda)$.

4. Conclusion

In this effort, a relatively large bio-optical dataset for the Southern Ocean was compiled to evaluate the performance of two widely used semi-analytical algorithms (QAA and GIOP) in the inversion of IOPs. To the best of our knowledge, this is the first systematic evaluation of both SAAs for waters in SO. Results of this effort show that both QAA and GIOP can provide overall satisfying retrievals of $a(\lambda)$ and $a_{ph}(\lambda)$, but there is a "twisted" pattern between the retrieved and measured $a_{dg}(\lambda)$. While it is always an ongoing effort to validate satellite products and improve remote sensing algorithms, results here advocate strong efforts to acquire high-quality field measurements for the evaluation, and improved inversion of $a_{dg}(\lambda)$ in the Southern Ocean.

Funding. National Natural Science Foundation of China (41941008); National Key Research and Development Program of China (2022YFC3104900, 2022YFC3104901).

Acknowledgments. Supports from all the cruise members of the 38th Chinese National Antarctic Research Expedition are greatly appreciated, which made it possible to collect the bio-optical properties in the Southern Ocean. The authors also want to thank all contributors to the GBD dataset and Dr. Valente for data compilation and for making the dataset publicly available.

Disclosures. The authors declare no conflicts of interest.

Data availability. Data underlying the results presented in this paper are not publicly available at this time but may be obtained from the authors upon request.

References

1. J. Moore and M. Abbott, "Phytoplankton chlorophyll distributions and primary production in the Southern Ocean," J. Geophys. Res. **105**(C12), 28709–28722 (2000).
2. K. Arrigo, D. Worthen, A. Schnell, *et al.*, "Primary production in Southern Ocean waters," J. Geophys. Res. **103**(C8), 15587–15600 (1998).
3. K. Arrigo, G. van Dijken, and S. Bushinsky, "Primary production in the Southern Ocean, 1997–2006," J. Geophys. Res. **113**, C8 (2008).
4. T. Frölicher, J. Sarmiento, D. Paynter, *et al.*, "Dominance of the Southern Ocean in anthropogenic carbon and heat uptake in CMIP5 models," J. Clim. **28**(2), 862–886 (2015).
5. P. Boyd, S. Doney, R. Strzepek, *et al.*, "Climate-mediated changes to mixed-layer properties in the Southern Ocean: assessing the phytoplankton response," Biogeosciences **5**(3), 847–864 (2008).
6. A. Constable, J. Melbourne-Thomas, S. Corney, *et al.*, "Climate change and Southern Ocean ecosystems I: how changes in physical habitats directly affect marine biota," Global Change Biol. **20**(10), 3004–3025 (2014).
7. L. Song, Z. Lee, S. Shang, *et al.*, "On the spatial and temporal variations of primary production in the South China Sea," IEEE Trans. Geosci. Remote Sensing **61**, 1–14 (2023).
8. Z. Lee, K. Carder, J. Marra, *et al.*, "Estimating primary production at depth from remote sensing," Appl. Opt. **35**(3), 463–474 (1996).
9. Z. Lee, V. Lance, S. Shang, *et al.*, "An assessment of optical properties and primary production derived from remote sensing in the Southern Ocean (SO GasEx)," J. Geophys. Res. **116**, C00F03 (2011).
10. D. Stramski, R. Reynolds, M. Kahru, *et al.*, "Estimation of particulate organic carbon in the ocean from satellite remote sensing," Science **285**(5425), 239–242 (1999).
11. H. Loisel, J. Nicolas, P. Deschamps, *et al.*, "Seasonal and inter-annual variability of particulate organic matter in the global ocean," Geophys. Res. Lett. **29**(24), 2196 (2002).
12. C. Fichot and R. Benner, "A novel method to estimate DOC concentrations from CDOM absorption coefficients in coastal waters," Geophys. Res. Lett. **38**(3), L03610 (2011).
13. X. Yu, F. Shen, and Y. Liu, "Light absorption properties of CDOM in the Changjiang (Yangtze) estuarine and coastal waters: An alternative approach for DOC estimation," Estuarine, Coastal Shelf Sci. **181**, 302–311 (2016).
14. H. Dierssen and R. Smith, "Bio-optical properties and remote sensing ocean color algorithms for Antarctic Peninsula waters," J. Geophys. Res. **105**(C11), 26301–26312 (2000).
15. M. Marrari, C. Hu, and K. Daly, "Validation of SeaWiFS chlorophyll a concentrations in the Southern Ocean: A revisit," Remote Sens. Environ. **105**(4), 367–375 (2006).
16. R. Johnson, P. Strutton, S. Wright, *et al.*, "Three improved satellite chlorophyll algorithms for the Southern Ocean," J. Geophys. Res. **118**(7), 3694–3703 (2013).
17. S. Chen, W. Smith Jr, and X. Yu, "Revisiting the ocean color algorithms for particulate organic carbon and chlorophyll-a concentrations in the Ross Sea," J. Geophys. Res. **126**(8), e2021JC017749 (2021).
18. IOCCG, *Remote Sensing of Inherent Optical Properties: Fundamentals, Tests of Algorithms, and Applications* Z. P. Lee (ed.), Reports of the International Ocean-Colour Coordinating Group No. 5, IOCCG, Dartmouth, Canada (2006).
19. P. Werdell, B. Franz, S. Bailey, *et al.*, "Generalized ocean color inversion model for retrieving marine inherent optical properties," Appl. Opt. **52**(10), 2019–2037 (2013).
20. S. Garver and D. Siegel, "Inherent optical property inversion of ocean color spectra and its biogeochemical interpretation: 1. Time series from the Sargasso Sea," J. Geophys. Res. **102**(C8), 18607–18625 (1997).
21. Z. Lee, K. L. Carder, C. D. Mobley, *et al.*, "Hyperspectral remote sensing for shallow waters: 2. Deriving bottom depths and water properties by optimization," Appl. Opt. **38**(18), 3831–3843 (1999).
22. C. Mouw, S. Greb, D. Aurin, *et al.*, "Aquatic color radiometry remote sensing of coastal and inland waters: Challenges and recommendations for future satellite missions," Remote Sens. Environ. **160**, 15–30 (2015).
23. Z. Lee, K. L. Carder, and R. A. Arnone, "Deriving inherent optical properties from water color: a multiband quasi-analytical algorithm for optically deep waters," Appl. Opt. **41**(27), 5755–5772 (2002).
24. S. Maritorena, D. A. Siegel, and A. R. Peterson, "Optimization of a semianalytical ocean color model for global-scale applications," Appl. Opt. **41**(15), 2705–2714 (2002).
25. X. Yu, M. S. Salama, F. Shen, *et al.*, "Retrieval of the diffuse attenuation coefficient from GOCI images using the 2SeaColor model: A case study in the Yangtze Estuary," Remote Sens. Environ. **175**, 109–119 (2016).
26. A. Valente, S. Sathyendranath, V. Brotas, *et al.*, "A compilation of global bio-optical in situ data for ocean colour satellite applications – version three," Earth Syst. Sci. Data **14**(12), 5737–5770 (2022).
27. J. Wei, Z. Lee, and S. Shang, "A system to measure the data quality of spectral remote-sensing reflectance of aquatic environments," J. Geophys. Res. **121**(11), 8189–8207 (2016).
28. IOCCG Protocol Series, "Protocols for satellite ocean color data validation: In situ optical radiometry," G. Zibordi, Z. Lee, S. Shang, *et al.*, eds., *IOCCG Ocean Optics and Biogeochemistry Protocols for Ocean Colour Sensor Validation*, Volume 3.0, IOCCG, Dartmouth, NS, Canada. (2019).
29. J. Mueller, A. Morel, R. Frouin, *et al.*, "Ocean Optics Protocols For Satellite Ocean Color Sensor Validation, Revision 4. Volume III: Radiometric Measurements and Data Analysis Protocols," *NTRS-NASA Technical Reports Server* (2003).
30. C. Mobley, "Estimation of the remote-sensing reflectance from above-surface measurements," Appl. Opt. **38**(36), 7442–7455 (1999).

31. Z. Lee, Y. Ahn, C. Mobley, *et al.*, "Removal of surface-reflected light for the measurement of remote-sensing reflectance from an above-surface platform," Opt. Express **18**(25), 26313–26324 (2010).
32. B. Mitchell, "Algorithms for determining the absorption coefficient for aquatic particulates using the quantitative filter technique," in *Ocean Optics X*, (SPIE, 1990), 137–148.
33. IOCCG Protocol Series, "Inherent Optical Property Measurements and Protocols: Absorption Coefficient," Neeley, A. and Mannino, A. (eds.),*IOCCG Ocean Optics and Biogeochemistry Protocols for Satellite Ocean Colour Sensor Validation*, Volume 1.0, IOCCG, Dartmouth, NS, Canada (2018).
34. S. Tassan and G. Ferrari, "An alternative approach to absorption measurements of aquatic particles retained on filters," Limnol. Oceanogr. **40**(8), 1358–1368 (1995).
35. S. Tassan and G. Ferrari, "A sensitivity analysis of the 'Transmittance-Reflectance' method for measuring light absorption by aquatic particles," J. Plankton Res. **24**(8), 757–774 (2002).
36. A. Mannino, M. Novak, N. Nelson, *et al.*, "*Measurement protocol of absorption by chromophoric dissolved organic matter (CDOM) and other dissolved materials*," IOCCG, Dartmouth, NS, Canada (2019).
37. R. Pope and E. Fry, "Absorption spectrum (380 –700 nm)of pure water. II. Integrating cavity measurements," Appl. Opt. **36**(33), 8710–8723 (1997).
38. Z. Lee, J. Wei, K. Voss, *et al.*, "Hyperspectral absorption coefficient of "pure" seawater in the range of 350-550 nm inverted from remote sensing reflectance," Appl. Opt. **54**(3), 546–558 (2015).
39. X. Yu, Z. Lee, J. Wei, *et al.*, "Impacts of pure seawater absorption coefficient on remotely sensed inherent optical properties in oligotrophic waters," Opt. Express **27**(24), 34974–34984 (2019).
40. G. Wei, Z. Lee, X. Wu, *et al.*, "Impact of temperature on absorption coefficient of pure seawater in the blue wavelengths inferred from satellite and in situ measurements," J. Remote Sens. **2021**, 1 (2021).
41. H. Gordon and M. Wang, "Retrieval of water-leaving radiance and aerosol optical thickness over the oceans with SeaWiFS: a preliminary algorithm," Appl. Opt. **33**(3), 443–452 (1994).
42. S. Bailey, B. Franz, and P. Werdell, "Estimation of near-infrared water-leaving reflectance for satellite ocean color data processing," Opt. Express **18**(7), 7521–7527 (2010).
43. S. Bailey and P. Werdell, "A multi-sensor approach for the on-orbit validation of ocean color satellite data products," Remote Sens. Environ. **102**(1-2), 12–23 (2006).
44. H. Gordon, O. Brown, R. Evans, *et al.*, "A semianalytic radiance model of Ocean Color," J. Geophys. Res. **93**(D9), 10909–10924 (1988).
45. C. D. Mobley, *Light, and Water: Radiative Transfer in Natural Waters* (Academic press, 1994).
46. Z. Lee and J. Tang, "The Two Faces of "Case-1" Water," J. Remote Sens. **2022**, 9 (2022).
47. X. Zhang, L. Hu, and M. He, "Scattering by pure seawater: effect of salinity," Opt. Express **17**(7), 5698–5710 (2009).
48. A. Bricaud, A. Morel, M. Babin, *et al.*, "Variations of light absorption by suspended particles with chlorophyll a concentration in oceanic (case 1) waters: Analysis and implications for bio-optical models," J. Geophys. Res. **103**(C13), 31033–31044 (1998).
49. J. O'Reilly and P. Werdell, "Chlorophyll algorithms for ocean color sensors-OC4, OC5 & OC6," Remote Sens. Environ. **229**, 32–47 (2019).
50. Z. Lee, C. Hu, S. Shang, *et al.*, "Penetration of UV-visible solar radiation in the global oceans: Insights from ocean color remote sensing," J. Geophys. Res. **118**(9), 4241–4255 (2013).
51. G. Zheng, D. Stramski, and R. A. Reynolds, "Evaluation of the Quasi-Analytical Algorithm for estimating the inherent optical properties of seawater from ocean color: Comparison of Arctic and lower-latitude waters," Remote Sens. Environ. **155**, 194–209 (2014).
52. L. Deng, W. Zhou, W. Cao, *et al.*, "Evaluating semi-analytical algorithms for estimating inherent optical properties in the South China Sea," Opt. Express **28**(9), 13155–13176 (2020).
53. X. Yu, Z. Lee, Z. Shang, *et al.*, "A simple and robust shade correction scheme for remote sensing reflectance obtained by the skylight-blocked approach," Opt. Express **29**(1), 470–486 (2021).
54. Z. Lee, R. Arnone, C. Hu, *et al.*, "Uncertainties of optical parameters and their propagations in an analytical ocean color inversion algorithm," Appl. Opt. **49**(3), 369–381 (2010).
55. X. Yu, Z. Lee, and W. Lai, "Global distribution of the spectral power coefficient of particulate backscattering coefficient obtained by a neural network scheme," Remote Sens. Environ. **296**, 113750 (2023).
56. A. Neeley, S. Freeman, and L. Harris, "Multi-method approach to quantify uncertainties in the measurements of light absorption by particles," Opt. Express **23**(24), 31043–31058 (2015).
57. D. Toole, D. Siegel, D. Menzies, *et al.*, "Remote-sensing reflectance determinations in the coastal ocean environment: impact of instrumental characteristics and environmental variability," Appl. Opt. **39**(3), 456–469 (2000).
58. G. Zibordi, F. Mélin, S. Hooker, *et al.*, "An autonomous above-water system for the validation of ocean color radiance data," IEEE Trans. Geosci. Remote Sensing **42**(2), 401–415 (2004).
59. Z. Lee, N. Pahlevan, Y.-H. Ahn, *et al.*, "Robust approach to directly measuring water-leaving radiance in the field," Appl. Opt. **52**(8), 1693–1701 (2013).
60. J. Wei, X. Yu, Z. Lee, *et al.*, "Improving low-quality satellite remote sensing reflectance at blue bands over coastal and inland waters," Remote Sens. Environ. **250**, 112029 (2020).
61. B. Barnes, J. Cannizzaro, D. English, *et al.*, "Validation of VIIRS and MODIS reflectance data in coastal and oceanic waters: An assessment of methods," Remote Sens. Environ **220**, 110–123 (2019).

62. M. Wang, X. Liu, L. Tan, *et al.*, "Impacts of VIIRS SDR performance on ocean color products," J. Geophys. Res.: Atmos. **118**, 10,347 (2013).
63. S. Hlaing, T. Harmel, A. Gilerson, *et al.*, "Evaluation of the VIIRS ocean color monitoring performance in coastal regions," Remote Sens. Environ **139**, 398–414 (2013).
64. B. Barnes and C. Hu, "Dependence of satellite ocean color data products on viewing angles: a comparison between SeaWiFS, MODIS, and VIIRS," Remote Sens. Environ **175**, 120–129 (2016).
65. C. Hu, B. Barnes, L. Qi, *et al.*, "A harmful algal bloom of Karenia brevis in the northeastern Gulf of Mexico as revealed by MODIS and VIIRS: a comparison," Sensors **15**(2), 2873–2887 (2015).
66. R. Li, M. Lewis, R. Gould Jr, *et al.*, "Inter-comparison between VIIRS and MODIS radiances and ocean color data products over the Chesapeake Bay," Remote Sens. **7**(2), 2193–2207 (2015).
67. Z. Lee, L. Zhao, C. Hu, *et al.*, "Absorption coefficient and chlorophyll concentration of oceanic waters estimated from band difference of satellite-measured remote sensing reflectance," J. Remote Sens. **3**, 0063 (2023).
68. D. Antoine, F. d'Ortenzio, S. Hooker, *et al.*, "Assessment of uncertainty in the ocean reflectance determined by three satellite ocean color sensors (MERIS, SeaWiFS and MODIS-A) at an offshore site in the Mediterranean Sea (BOUSSOLE project)," J. Geophys. Res. **113**(C7), C07013 (2008).
69. G. Zibordi, J. Berthon, F. Mélin, *et al.*, "Validation of satellite ocean color primary products at optically complex coastal sites: Northern Adriatic Sea, Northern Baltic Proper and Gulf of Finland," Remote Sens. Environ. **113**(12), 2574–2591 (2009).
70. P. Werdell and S. Bailey, "An improved in-situ bio-optical data set for ocean color algorithm development and satellite data product validation," Remote Sens. Environ. **98**(1), 122–140 (2005).